

Optical polarization map of the Polaris Flare with RoboPol

G. Panopoulou^{1,2*}, K. Tassis^{1,2*}, D. Blinov^{1,7}, V. Pavlidou^{1,2}, O. G. King³,
 E. Paleologou¹, A. Ramaprakash⁴, E. Angelakis⁵, M. Baloković³, H. K. Das⁴,
 R. Feiler⁶, T. Hovatta^{3,8}, P. Khodade⁴, S. Kiehlmann⁵, A. Kus⁶, N. Kylafis^{1,2},
 I. Liodakis¹, A. Mahabal³, D. Modi⁴, I. Myserlis⁵, I. Papadakis^{1,2}, I. Papamastorakis^{1,2},
 B. Pazderska⁶, E. Pazderski⁶, T. J. Pearson³, C. Rajarshi⁴, A. C. S. Readhead³,
 P. Reig^{2,1}, J. A. Zensus⁵

¹*Department of Physics and ITCPT, University of Crete, 71003, Heraklion, Greece*

²*Foundation for Research and Technology - Hellas, IESL, Voutes, 7110 Heraklion, Greece*

³*Cahill Center for Astronomy and Astrophysics, California Institute of Technology, 1200 E California Blvd, MC 249-17, Pasadena CA, 91125, USA*

⁴*Inter-University Centre for Astronomy and Astrophysics, Post Bag 4, Ganeshkhind, Pune - 411 007, India*

⁵*Max-Planck-Institut für Radioastronomie, Auf dem Hügel 69, 53121 Bonn, Germany*

⁶*Toruń Centre for Astronomy, Nicolaus Copernicus University, Faculty of Physics, Astronomy and Informatics, Grudziadzka 5, 87-100 Toruń, Poland*

⁷*Astronomical Institute, St. Petersburg State University, Universitetsky pr. 28, Petrodvoretz, 198504 St. Petersburg, Russia*

⁸*Aalto University Metsähovi Radio Observatory, Metsähovintie 114, 02540 Kylmälä, Finland*

8 February 2019

ABSTRACT

The stages before the formation of stars in molecular clouds are poorly understood. Insights can be gained by studying the properties of quiescent clouds, such as their magnetic field structure. The plane-of-the-sky orientation of the field can be traced by polarized starlight. We present the first extended, wide-field (~ 10 deg²) map of the Polaris Flare cloud in dust-absorption induced optical polarization of background stars, using the RoboPol polarimeter at the Skinakas Observatory. This is the first application of the wide-field imaging capabilities of RoboPol. The data were taken in the R-band and analysed with the automated reduction pipeline of the instrument. We present in detail optimizations in the reduction pipeline specific to wide-field observations. Our analysis resulted in reliable measurements of 641 stars with median fractional linear polarization 1.3%. The projected magnetic field shows a large scale ordered pattern. At high longitudes it appears to align with faint striations seen in the *Herschel*-SPIRE map of dust emission (250 μm), while in the central 4-5 deg² it shows an eddy-like feature. The overall polarization pattern we obtain is in good agreement with large scale measurements by Planck of the dust emission polarization in the same area of the sky.

Key words: stars: formation – ISM: clouds – ISM: individual objects (Polaris Flare) – polarization.

1 INTRODUCTION

Molecular clouds in their vast complexity hold the key to understanding the early stages of the star formation process. Magnetic fields and turbulence are the two main mecha-

nisms that dictate the structural, dynamical and evolutionary properties of these clouds, through their competition against gravity. Their role in the onset of star formation can be studied best in quiescent non-star-forming regions, where stellar feedback is not present. One such region is the Polaris Flare, a translucent high-latitude molecular cloud first observed by Heiles (1984). Estimates of the cloud's distance vary from 130 pc – 240 pc (Heithausen et al. 1993) to 380 ± 40 pc (Schlafly et al. 2014). It is believed to be in the early stages of its formation, since it does not exhibit

* Contact authors' e-mail addresses: panopg@physics.uoc.gr (GP); tassiss@physics.uoc.gr (KT)

† Institute for Theoretical and Computational Physics, formerly Institute for Plasma Physics

any signs of active star formation (Ward-Thompson et al. 2010). CO observations have provided invaluable information on the turbulence signatures in the densest parts of the cloud (Falgarone et al. 1998; Hily-Blant & Falgarone 2009). The *Herschel* space telescope mapped over 15 deg^2 of the cloud in dust emission as part of the *Herschel* Gould Belt Survey (André et al. 2010; Miville-Deschênes et al. 2010).

The structure of the magnetic field of a cloud, as projected on the plane of the sky, can be probed by observing polarized radiation. The polarization of starlight transmitted through a cloud is believed to be caused by dichroic extinction due to aspherical dust grains that are partially aligned with the magnetic field. This alignment causes the polarization direction of the light of background stars to trace the magnetic field direction of the cloud as projected on the plane of the sky. The same alignment process causes the thermal emission of these dust grains to be polarized in the direction perpendicular to the magnetic field.

Information on the plane-of-the-sky magnetic field of the Polaris Flare was recently provided for the first time through polarized dust emission (Planck collaboration XIX 2015; Planck collaboration XX 2015). These data, however, are limited by the instrumental resolution and confusion along the line of sight. A mapping of the region in polarized starlight, which is complementary to the dust emission but suffers from different limitations, is necessary to resolve these issues.

We obtained optical polarization measurements of stars projected on 10 deg^2 of the Polaris Flare region with RoboPol. The RoboPol instrument is a 4-channel optical polarimeter with no moving parts, other than a filter wheel (Ramaprakash et al., in prep). It can measure both linear fractional Stokes parameters $q = Q/I$ and $u = U/I$ simultaneously, thus avoiding errors caused by the imperfect alignment of rotating optical elements and sky changes between measurements (polarization, seeing conditions).

Each star in the field of view creates four images (spots) on the CCD displaced symmetrically in the horizontal and vertical directions. A mask supported by four legs is positioned at the centre of the field of view. This allows targets that are centred on the mask to be measured with four times lower sky noise than the rest of the field. A typical image seen with RoboPol is shown in Fig. 1. The instrument has a $13' \times 13'$ field of view, enabling the rapid polarimetric mapping of large areas of the sky. RoboPol is equipped with standard Johnson-Cousins *R*- and *I*-band filters and is mounted on the 1.3-m, $f/7.7$ Ritchey-Crétien telescope at Skinakas Observatory in Crete, Greece. It has been operating since May 2013.

RoboPol has been monitoring the optical linear polarization of a large sample of gamma-ray bright blazars for the past two years (Pavlidou et al. 2014). In addition, the instrument is being used for long-term monitoring of Be X-ray binaries (Reig et al. 2014). Observations of optical afterglows of gamma-ray bursts have also been conducted with RoboPol (King et al. 2014). More complete descriptions of the instrument and data reduction pipeline are given in Ramaprakash et al. (in prep.) and King et al. (2014), respectively.

The data presented here are the first obtained from an analysis of the instrument’s entire field of view. We present the observational details in Section 2. In Section 3 we de-

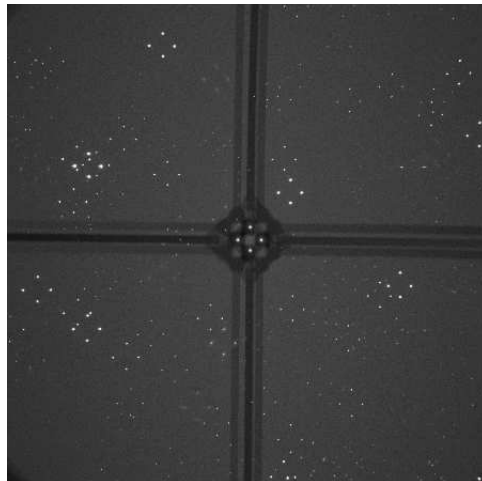


Figure 1. A field observed by RoboPol. Each star in the field creates a quadruplet of images (spots) on the CCD. The central dark region is the mask used for lowering sky noise for the target at the centre of the field of view and the cross-like figure is created by the mask-supporting legs.

scribe the methods used for analysing sources in the entire field of view. We present and discuss the results of our observations in Section 4 and summarize our findings in Section 5.

2 OBSERVATIONS

Polarimetric observations were taken during 25 nights from August to November 2013, totaling around 60 hours of telescope time. The observations covered an area of 10 deg^2 : $l = [122.6^\circ, 126.0^\circ]$, $b = [24.7^\circ, 27.9^\circ]$. The area was initially divided into 275 non-overlapping fields spaced 13.2 arcminutes apart (slightly larger than the size of the RoboPol field of view). Of them, 227 were observed by the end of the period. The number of observations of each field ranges between 2 and 6, with 93% of all fields having been observed at least 3 times. 95% of the exposures were 180 seconds long, while the remaining were 120 seconds long. All observations were taken in the R band.

3 ANALYSIS

Previous studies with RoboPol concentrated on sources either exclusively within the mask, or with the addition of some selected sources in the field of view around the central target. Although the data reduction pipeline presented by King et al. (2014) was designed for the entire RoboPol field of view, its implementation in this particular project showed the need for some adjustments and additions. Sources outside the mask present a number of challenges. Some are common in most polarimetric studies in the optical, while others are due to the particular design of the instrument. A measurement may be adversely affected by one of the following sources of systematic error:

- Large-scale optical aberrations
- Proximity to the mask and its legs

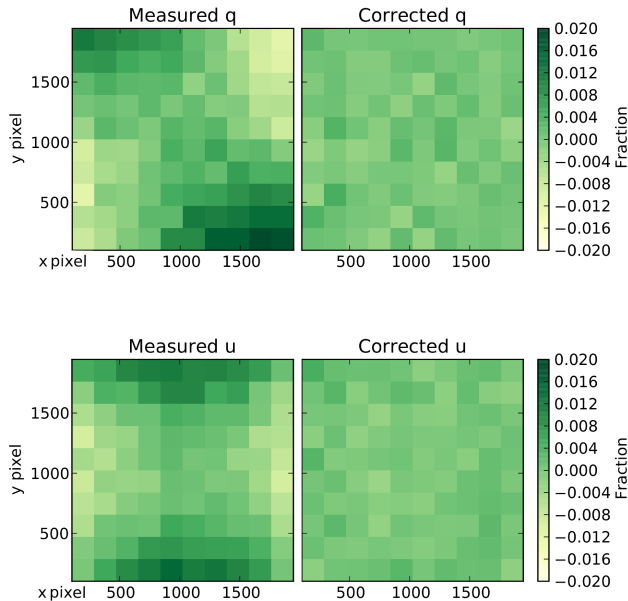


Figure 2. Relative Stokes parameters across the CCD. Left: measured q (top) and u (bottom). Right: residual q (top) and u (bottom) after subtracting the fitted model. Each square panel shows values on the CCD binned in 100 cells. Each cell is colored according to its average value.

- Proximity to the CCD edge
- Proximity to other sources
- Selection of apertures for photometry
- Dust on optical elements

An additional systematic error has already been identified and discussed by King et al. (2014). A rotation in the polarization reference frame of the telescope with respect to that of the sky causes all angles to be larger by $2.31^\circ \pm 0.34^\circ$. All polarization angle measurements presented in this paper have been corrected for this.

This section outlines the analysis of observations and the methodology adopted to control these systematic effects.

3.1 Significance of measurements and debiasing

The measurement of the fractional linear polarization (p) at the low polarization regime which is relevant for interstellar polarization, being always positive, is biased towards values larger than the true (intrinsic) polarization (Simmons & Stewart 1985). Thus, p measurements should be debiased to find their most probable intrinsic value. In the analysis, we consider only sources with signal-to-noise ratios ($p/\sigma_p \geq 2.5$) so that errors are approximately normally distributed. The maximum-likelihood estimator of the true value of p found by Vaillancourt (2006) for measurements with $p/\sigma_p \geq 3$ significance is:

$$p_d = \sqrt{p^2 - \sigma_p^2} \quad (1)$$

We extend this formula to $p/\sigma_p \geq 2.5$ and use it to debias all measurements of p .

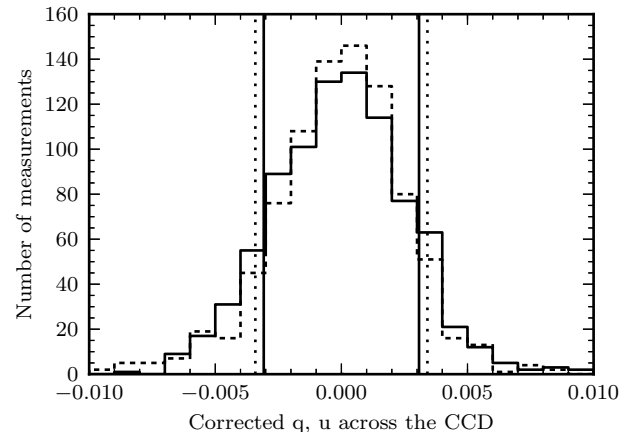


Figure 3. Distributions of the residuals of q and u across the CCD, after the subtraction of the model fit (q : dotted, u : solid). The vertical lines show the standard deviation of each distribution.

3.2 Large-scale optical aberrations

Large-scale aberrations caused by the optical system are corrected by the instrument model, as presented by King et al. (2014). The model is created by placing an unpolarized standard star at many positions across the field of view and finding the best-fitting parameters that cancel the global, instrumentally-induced polarization and vignetting.

The instrument model has been found to perform equally well, regardless of telescope pointing position (which may result in different telescope stresses) and after multiple removals and re-installations of the instrument on the telescope. The set of models that were created for these tests have been combined into one with improved performance with respect to that presented by King et al. (2014). Below we estimate the systematic uncertainty that remains after the model correction.

3.2.1 Systematic uncertainty from model residuals

Fig. 2 shows the uncorrected (left) and corrected (right) q (top) and u (bottom) values across the CCD derived by using this combined model. The data are binned in 100 cells of 39 arcsec width and the mean value is plotted in each one. On average, 2.4 star measurements contribute to each cell. The residuals appear to be homogeneous across the CCD.

The distributions of residual q and u of the combined model are shown in Fig. 3. Vertical lines show the standard deviation of each distribution ($\sigma_{q,\text{res}} = 0.0034$, $\sigma_{u,\text{res}} = 0.0031$). Statistical errors of measurements of unpolarized standards are an order of magnitude lower than these standard deviations, thus their contribution to this scatter can be ignored. Therefore, we take the systematic uncertainties in q and u to be $\sigma_{q,\text{sys}} = \sigma_{q,\text{res}}$, $\sigma_{u,\text{sys}} = \sigma_{u,\text{res}}$.

From now on, in order to estimate total uncertainties in q and u , we add statistical and systematic uncertainties in quadrature,

$$\sigma_q^2 = \sigma_{q,\text{sys}}^2 + \sigma_{q,\text{stat}}^2 \quad (2)$$

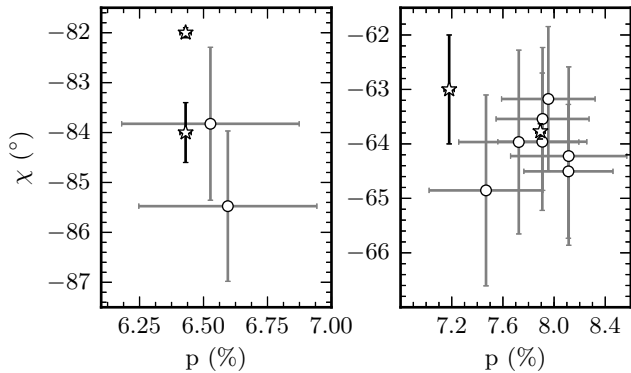


Figure 4. EVPA versus fractional linear polarization of standard stars. Left: BD+59.389, right: VI Cyg12. Literature values are shown by stars (see references in Table 1) and circles are measurements outside the mask. Error bars include the statistical and systematic uncertainties added in quadrature.

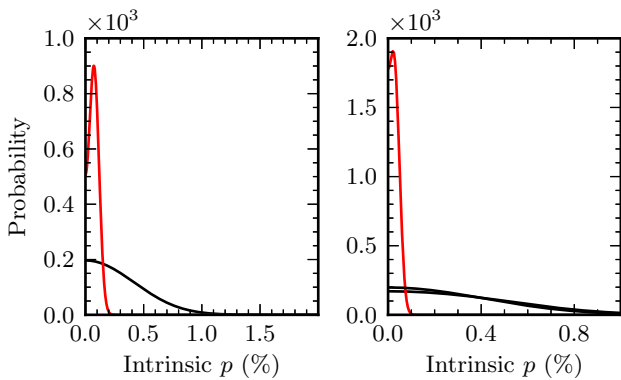


Figure 5. Probability distribution of the intrinsic value of p of unpolarized standards, given the measurement in the literature (red) and our own (black). Left: HD151406, right: HD212311. There are two black lines (measurements) of HD212311.

$$\sigma_u^2 = \sigma_{u,\text{sys}}^2 + \sigma_{u,\text{stat}}^2. \quad (3)$$

The total uncertainty in q and u can be propagated to find the total uncertainty in fractional linear polarization (p) and electric vector position angles (EVPA or χ) using the equations:

$$p = \sqrt{q^2 + u^2}, \quad \sigma_p = \sqrt{\frac{q^2 \sigma_q^2 + u^2 \sigma_u^2}{q^2 + u^2}} \quad (4)$$

$$\chi = \frac{1}{2} \tan^{-1} \frac{u}{q}, \quad \sigma_\chi = \frac{1}{2} \sqrt{\frac{u^2 \sigma_q^2 + q^2 \sigma_u^2}{(q^2 + u^2)^2}} \quad (5)$$

Assuming low polarization the expression for $\sigma_{\chi,\text{sys}}$ can be written as:

$$\sigma_\chi \simeq \frac{1}{2} \frac{\sigma_p}{p}. \quad (6)$$

3.2.2 Performance: Standard Stars

To assess the accuracy of the instrument model, measurements of stars with known polarization values were taken

and were then compared to the literature. During the two observing seasons, a number of standard stars (different from the ones used for the model calculation) were observed throughout the field of view. Catalog measurements as well as the band in which they were taken are shown in Table 1. Measurements of the unpolarized stars in the R band could not be found, so those in other bands are quoted.

Fig. 4 presents RoboPol measurements of polarized standards (denoted by circles) and their literature values (stars) on the EVPA - polarization fraction plane. All p measurements are consistent with the literature within the errors (which include both the statistical and systematic uncertainties discussed above). Measurements of p have not been debiased.

In the case of unpolarized stars, biasing of p measurements is very pronounced and the interpretation of the measurement uncertainty is not straightforward. To facilitate comparison of our measurements with literature values, we plot, in Fig. 5, the probability distribution (likelihood) of the intrinsic (true) value of p , given the literature measurement (red) and our own (black). This likelihood function (see Vaillancourt (2006), equation 8) takes into account that the measured values of p follow a Rice, rather than a normal, distribution. In calculating the likelihood function we have used a total uncertainty obtained by adding statistical and systematic uncertainties in quadrature, as in equations (2) and (3). In both cases, our measurements are consistent within uncertainties with the literature measurements. There are two measurements (black lines) of the standard HD212311. For unpolarized standards the EVPA does not carry meaningful information, as can be seen by substituting $\sigma_p/p > 1$ into equation (5): $\sigma_\chi \geq 30^\circ$.

3.3 Proximity to the mask, legs and CCD edge

The mask and its supporting legs cast shadows on specific regions of the CCD rendering them unusable. Therefore, sources that happen to fall in the shadow of the mask legs or within 155 pixels (radially) of the mask centre are not considered in the analysis.

Sources falling very close to any of the CCD edges are very likely to suffer partial photon losses. Also, light reaching these areas is subject to large optical distortions. Since the typical separation between a pair of the four images is 100 pixels, we reject any spot within 100 pixels of the edges from the analysis.

3.4 Proximity to other sources

Sometimes images from different stars happen to fall within a few pixels of each other on the CCD. Since the typical diameter of a spot is 8 pixels (3.2 arcsec), photons from both spots are blended, as shown in Fig. 6. The relative Stokes parameters are computed using the following equations:

$$q = \frac{N_1 - N_0}{N_1 + N_0}, \quad \sigma_q = \sqrt{\frac{4(N_1^2 \sigma_0^2 + N_0^2 \sigma_1^2)}{(N_0 + N_1)^4}} \quad (7)$$

$$u = \frac{N_3 - N_2}{N_3 + N_2}, \quad \sigma_u = \sqrt{\frac{4(N_3^2 \sigma_2^2 + N_2^2 \sigma_3^2)}{(N_2 + N_3)^4}} \quad (8)$$

Table 1. Polarization standard stars shown in Fig. 4

	BD+59.389	VICyg12	HD151406	HD212311
P (%)	6.430 \pm 0.022 6.43 \pm 0.13	7.893 \pm 0.037 7.18 \pm 0.04	0.085 \pm 0.041	0.034 \pm 0.021 0.02 \pm 0.021 0.045
χ ($^\circ$)	98.14 \pm 0.10 96.0 \pm 0.6	116.23 \pm 0.14 117 \pm 1	-2	50.99 36.2 \pm 51.3 10.4
Band	R	R	no filter	V
Reference	1, 5	1, 3	2	1, 4, 5

1 - Schmidt, Elston & Lupie (1992), 2 - Berdyugin, Pirola & Teerikorpi (2014), 3 - Bailey & Hough (1982), 4 - Heiles (2000), 5 - Eswaraiah et al. (2011)

where N_i is the number of photons in the i^{th} spot and σ_i is the uncertainty that results from the photon noise. Therefore, overlapping of spots causes an artificially large difference in intensity of one pair of spots belonging to each affected star. The two the point spread functions (PSFs) cannot be de-blended, since the pipeline performs aperture photometry. Typically, this contamination results in erroneously large degrees of polarization (but not necessarily, this can vary based on the relative brightness of the sources involved) and, most notably, regular EVPAs (0° , $\pm 45^\circ$, $\pm 90^\circ$). This follows from the definition of the EVPA, equation (5). If one of the vertical images of the star is artificially brightened, for example $N_1 \ll N_0$, then $|u| \ll |q| \Rightarrow \chi \rightarrow 0^\circ, \pm 90^\circ$. Whereas if one of the horizontal images is affected by a nearby source, e.g. $N_2 \ll N_3$, then $|q| \ll |u| \Rightarrow \chi \rightarrow \pm 45^\circ$. Fig 7 (left) shows the EVPA versus fractional linear polarization of all sources with at least 2 measurements found in the Polaris Flare field (5172 in total). Measurements of $p > 20\%$ are clustered around regular EVPAs - the clear signature of nearby star contamination.

We remove such sources from the analysis in the following way. If any of the four spots of a star suffers from confusion with another spot then we flag it as nearby contaminated. This flag applies if a source exists within $3 \times \text{FWHM}$ of a star spot. In cases where the spots of two stars happen to fall exactly on each other and are identified as a single source we check if any spot is assigned to more than one star. The effect of removing contaminated sources from the final catalog can be seen in Fig. 7 (right). All but two measurements with $p > 20\%$ were caused by proximity to other sources.

Stars that are affected by reflections, and even other close-by stars in the case that the previous check fails, can be removed by checking the ratio of the FWHM between two pairs of spots. The distribution of these ratios for all stars found in all observed frames is shown in Fig. 8. We discard measurements lying outside the range 0.87 to 1.15 (vertical lines).

3.5 Aperture optimization

The RoboPol pipeline performs aperture photometry to measure the intensity (photon counts - N) of each spot. It then uses these values to calculate the Stokes parameters as shown in equations (7) and (8). Photometry measurements are greatly affected by the choice of aperture size (e.g. Howell 1989). If the aperture is too large the value ob-

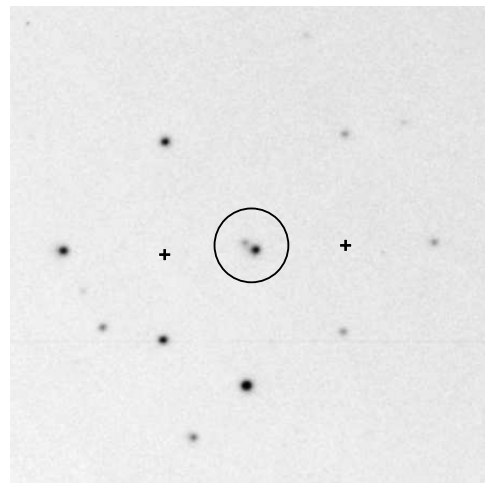


Figure 6. An example of sources that are affecting each other's measurements due to their proximity (circled spots). The positions of these stars (centres of quadruplets) are shown with crosses.

tained suffers from background contamination and the signal to noise ratio is decreased. On the other hand, if the aperture is too small only a fraction of the total flux is measured. This is not a problem if the same fraction of photons are counted, since polarimetric measurements depend on the relative brightness of two spots. If, however, the PSFs of two spots belonging to a source are different, then the fraction of the total flux measured is not the same and this introduces artificial polarization.

A number of circumstances may affect the PSF of the four spots of a source. Bad seeing or weather conditions (wind) sometimes cause sources to appear elongated instead of round. Also, the optical system of the instrument may distort the shape of the PSF and mainly the wings of the profile. Typically, bright stars (whose wings are more prominent) are affected more severely than faint ones. Therefore, it is essential that photometry be performed with an aperture optimized for each source. Also, the complexity of the optical system introduces some asymmetries in the PSFs of the vertical and horizontal images of a star. Consequently, photometry must also be optimized for *each* of the four images of a star.

We created a simple aperture optimization algorithm as an addition to the original pipeline, presented in King et al. (2014). Photon counts are measured within a circular aper-

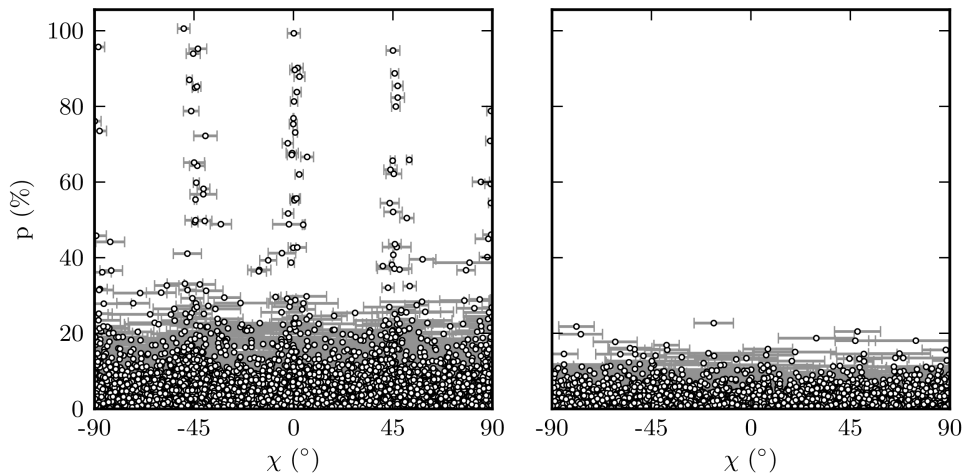


Figure 7. Fractional linear polarization versus EVPA for stars in the Polaris Flare field. Left: Measurements at regular angles (0° , $\pm 45^\circ$, $\pm 90^\circ$) are caused by nearby contamination as seen in Fig. 6. Right: Measurements that survive after the removal of stars that suffered this contamination. Most remaining measurements of $p > 5\%$ are caused by other systematics.

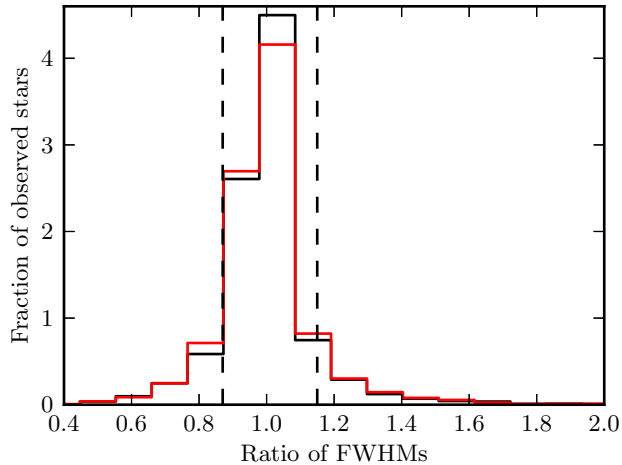


Figure 8. Distributions of ratios of the FWHM between vertical (black) and horizontal (red) spots for a number of fields. Vertical lines mark the area that contains acceptable ratios.

ture centred on each spot, while the background level is estimated within an outer concentric annulus that is separated from the inner aperture by a gap. The diameter of the background annulus is a constant multiple of the aperture size. The constant is different for faint and bright sources as the latter have more extended wings, so that the annulus does not contain any light from the source while retaining the smallest possible distance from the source for the background estimation.

By measuring the background subtracted photon flux within increasing apertures we create a growth curve for each spot. Each of the four growth curves of the source are fitted with a fourth degree polynomial, $P(x)$ (no errors are accounted for in the fit). The size of the aperture at which the normalized photon flux saturates is the optimum. To locate it in practice we look for the aperture size at which the rate of photon flux increase has reached some small value λ . In other words, the optimal aperture is the root of the

equation:

$$\frac{dP}{dx} = \lambda P(x). \quad (9)$$

An example growth curve of one of the images of a star is shown in Fig. 9 (circles) along with its polynomial fit (solid line). The dashed vertical line shows the optimal aperture found by solving equation (9). This aperture is used to measure the photon counts and noise (N , σ) of this spot. The optimization is used for all data, including those collected for the instrument model calculation.

The choice of the value for λ

To calibrate equation (9) and determine the best value of λ , we created growth curves of polarization standard stars that were routinely observed in the field and measured their fractional linear polarizations and angles using all the different aperture sizes. Fig. 10 shows the fractional linear polarization (top) and EVPA (middle) measured for VI Cyg12 with different apertures. As the aperture increases, these quantities saturate at some value consistent with those found in the literature (gray bands). As aperture size continues to increase, the signal-to-noise ratio worsens and also nearby sources may affect the measurement. The point on the horizontal axis after which saturation occurs is the optimal aperture for this star. The parameter λ was selected so that it reflects this transition. The bottom panel of Fig. 10 shows the four growth curves of VI Cyg12 and the corresponding polynomial fits. The vertical line shows the aperture that was chosen as optimal.

Because the standards observed with RoboPol are bright (typically 9-11 mag) we needed to extend this sample to stars of lower brightness. We selected 6 stars that were already observed in the field and observed them in the mask. We used the values found in the mask to define the optimal aperture for these sources when observed in the field. Finally, we optimized the parameter λ so that it yields an accurate optimal aperture for most of the stars (both these 6 as well as the standards): $\lambda = 0.02$.

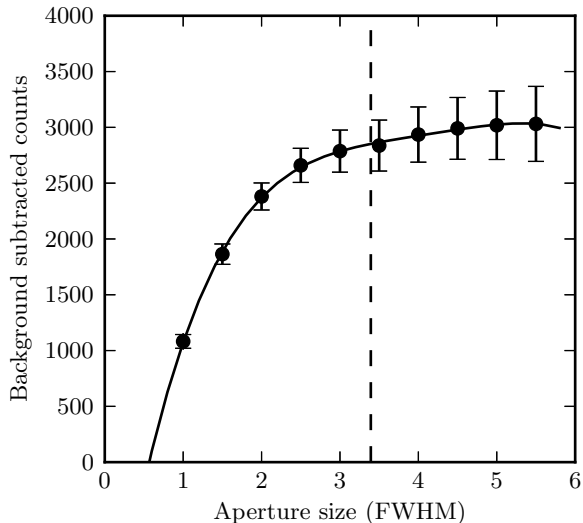


Figure 9. Growth curve of one of the images of a star (circles show the number of background subtracted counts for each aperture size). A fourth degree polynomial is fit to the points. The optimal aperture is shown with the dashed line.

3.6 Detection of dust specks using flat field images

The design of RoboPol does not allow us to correct science images for irregularities in transmission and uneven sensitivity throughout the field in conventional ways (e.g. by dividing pixel-by-pixel by a flat field image). Because both sets of orthogonally polarized beams are projected on the same CCD, when recording an extended image (such as a flat) each point on the CCD is exposed to four rays tracing four different optical paths through the instrument. In contrast, the photon counts we would like to correct (i.e. each of the four images corresponding to a point source) arrive on the CCD through a single optical path since each beam corresponds to a different orientation of the plane of polarization. Light from the sky against which they are projected still arrives through four paths for each pixel, but at different ratios, since the polarization of the sky differs between the moments of science and flat field image acquisition. This makes ordinary flat fielding impossible.

The global non-uniformity of the field (caused by vignetting) is corrected by the instrument model as described in Section 3.2.2. Small-scale non-uniformities cannot be corrected for, but they can be identified on flat-field images. Stars that happen to be affected by these small scale variations must be excluded from the analysis. An example is shown in Fig. 11 where the crescent pattern produced by a dust speck is clearly visible in the exposure and coincides with one of the four spots of a star (circled in white).

We process flat-field images obtained in the evening and/or the morning of each night in the following way: we create a master flat by normalizing separate shots and taking the median. After that we fit a third degree polynomial to the master flat and subtract its value from each pixel, thus removing the large scale vignetting in the flat image.

At the position of each spot in the science image, we

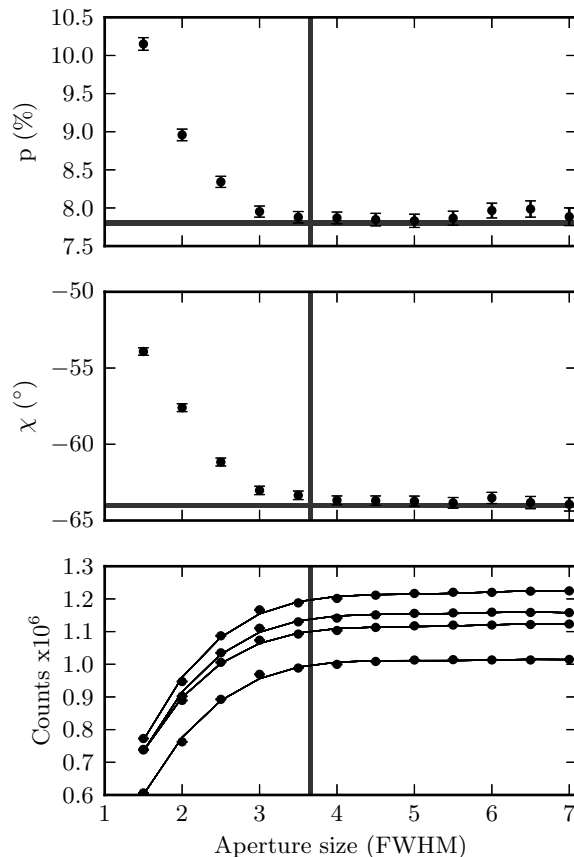


Figure 10. Top: Fractional linear polarization of the standard star VI Cyg12 measured with different aperture sizes (multiples of FWHM). The horizontal gray band shows the literature value $\pm 1\sigma$. The position of the vertical gray band shows the mean of the four optimal apertures while its width represents their scatter. Middle: EVPA measured with different aperture sizes. Bottom: Background subtracted number of counts with different aperture sizes (growth curve). The growth curves for all four of images of the star are shown, along with a fourth degree polynomial fit.

calculate the mode value (F_{bgr}) and standard deviation of counts (σ_{bgr}) of pixels on the flat-field image that fall within an aperture with diameter equal to the background annulus. In principle, by comparing these quantities on all four spots of a star we can determine whether any of them has fallen on a dust speck, since this would cause significant variations in F_{bgr} and σ_{bgr} .

To establish a set of reliable criteria that can identify most, if not all, dust-contaminated stars we analysed data of the Be X-ray binary CepX4 (e.g. Ulmer et al. 1973), which is one of the most crowded fields observed with RoboPol (Reig et al. 2014). We constructed a number of different quantities with the information from the flat field image. Those that proved most useful in revealing the effect of dust contamination were the following:

- difference between the σ_{bgr} of a star's vertical (horizontal) spots ($\Delta\sigma_{\text{bgr,v}}, \Delta\sigma_{\text{bgr,h}}$),
- difference between the background value of a star's vertical (horizontal) spots ($\Delta F_{\text{bgr,v}}, \Delta F_{\text{bgr,h}}$),
- maximum σ_{bgr} (among four spots),
- minimum σ_{bgr} (among four spots).

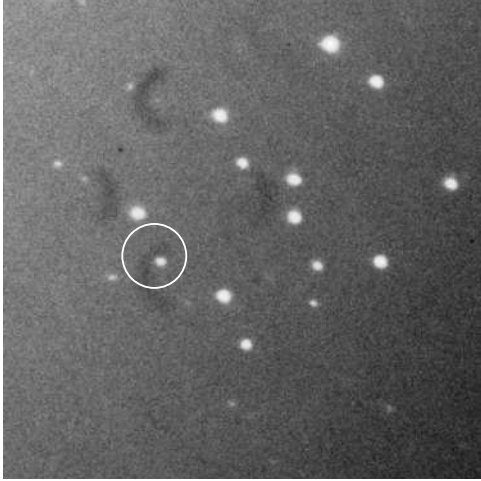


Figure 11. Crescent dust patterns on the CCD. One of the four images of a star falls on a dust pattern (in the white circle).

The distributions of all 6 quantities are shown in Fig. 12. These quantities are measured in units of normalized counts in the processed master flat image. The outliers of these distributions are stars that coincide with the most prominent dust specks. According to these distributions we selected the thresholds depicted by vertical lines in Fig. 12.

Using these criteria we manage to eliminate only stars that are affected by the most obvious dust shadows. A more sophisticated analysis is needed to identify more subtle anomalies on the CCD.

3.7 Statistical assessment

The standard observing strategy in the RoboPol project is to obtain multiple exposures of the same field. We are thus able to use the stability of the measurements (in a statistical sense) to further reject stars with unreliable polarization measurements. One reason for turning to a statistical treatment of the data is that even after the first stage of rigorous cuts described in this section, some systematic errors are still present. These include faint dust specks, reflections from bright stars, and in general, sources with properties around the various thresholds that were used.

First, we choose to work with stars that have reliable measurements of the weighted mean of p ($\bar{p}/\bar{\sigma}_p \geq 2.5$). The weighted mean is calculated by substituting into equation (4) the weighted mean q and u values of a star.

One way to quantify the statistical significance of the differences between the n measurements of a star is by computing the reduced χ^2 (χ_{red}^2) of all of its q and u measurements:

$$\chi_{red,q}^2 = \frac{1}{n-1} \sum_{j=1}^n \frac{(q_j - \bar{q})^2}{(\sigma_{q,j})^2} \quad (10)$$

and similarly for $\chi_{red,u}^2$. By placing a threshold in the value χ_{red}^2 we can eliminate stars that deviate from the expected normal behavior. The threshold was selected so as to remove the tail of the distribution of all χ_{red}^2 values of stars in the Polaris Flare region. The distributions of these values for q and u measurements are shown in Fig. 13 as well as the selected threshold (vertical line).

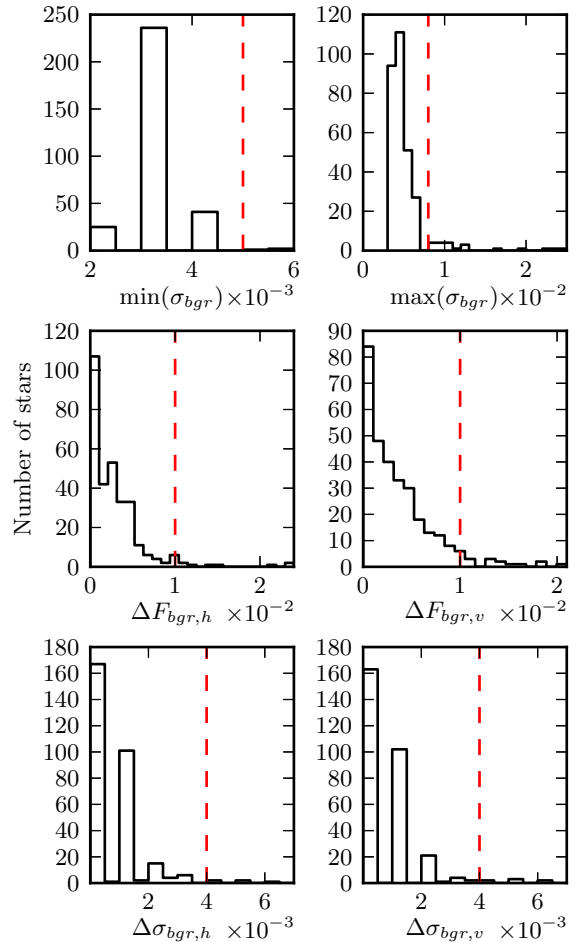


Figure 12. Distributions of the values extracted from the flat fields and used for identifying dust specks. Values on the horizontal axis are measured in normalized counts.

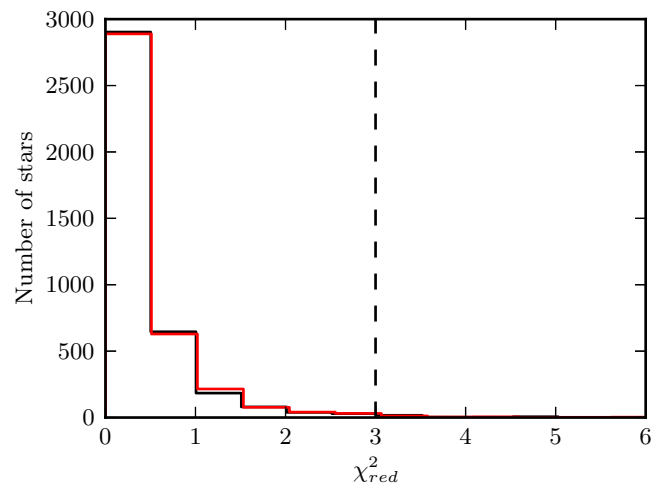


Figure 13. Distributions of χ_{red}^2 of q (black) and u (red) of stars with $\bar{p}/\bar{\sigma}_p \geq 2.5$. The vertical line shows the selected threshold.

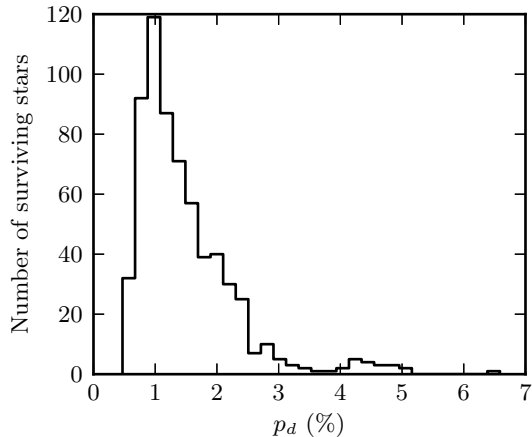


Figure 14. Distribution of debiased fractional linear polarizations of all 641 sources resulting from the analysis.

Stars that still remain after these cuts and show signs of some type of contamination visible by eye on the raw science images were removed by hand. These include types of contamination already presented in this section as well as projected double stars, for which the analysis does not account.

4 RESULTS AND DISCUSSION

The analysis provides us with 641 stars with reliable p and χ measurements. The distribution of debiased fractional linear polarizations of all these sources is shown in Fig. 14. The median of the distribution is at 1.3%. Fig. 15 shows the debiased polarization percentage against visual extinction (A_V) taken from the NASA/IPAC Extragalactic Database (NED) which uses the Schlafly & Finkbeiner (2011) extinction map. The dashed line shows the empirically determined upper limit in polarization at a given A_V : $p/A_V = 0.03$ (Serkowski, Mathewson & Ford 1975). We mark sources above this limit with empty circles and use this line as a threshold. Sources above the line are considered separately as their polarizations may have an intrinsic contribution.

In order to construct the polarization map of the region we transform all EVPAs (measured with respect to the North-South celestial pole direction) into galactic angles according to Stephens et al. (2011). In Fig. 16 we plot the polarization segments of all stars below the $p_d - A_V$ line of Fig. 15 at each star position on the *Herschel*-SPIRE 250 μm image¹ of the Polaris Flare (André et al. 2010). The length of each segment is proportional to the debiased p of the star, calculated using equation (1). These measurements are presented in the online table accompanying this paper (Table 2).

The most striking feature of the polarization map is the extended ordered pattern at large longitudes. In this region the plane-of-the-sky magnetic field appears to be oriented in

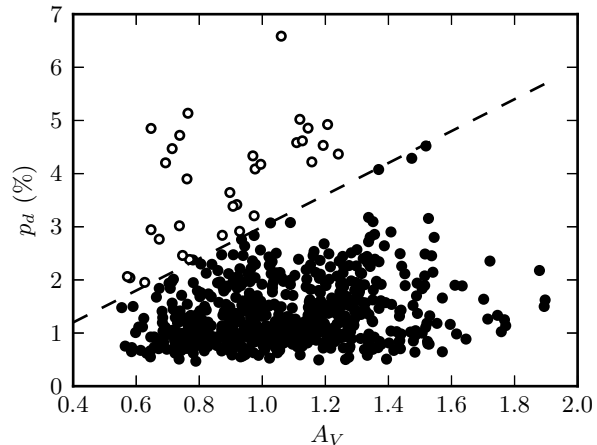


Figure 15. Debiased polarization percentage vs. visual extinction, A_V for all our reliably measured stars. The dashed line shows the maximum observable p at all A_V ($p = 0.03A_V$). Stars above the black line are marked with empty circles.

approximately the same direction as that of the faint striations seen in dust emission. The projected magnetic field in the top part of the map seems to turn to meet the orientation of the ordered region towards smaller latitudes. Segments at the largest longitudes are mostly parallel to lines of constant longitude, following the projected curvature of a vertical cloud structure that is partly cut-off by the map edges. A border appears to exist, spanning the diagonal of region $(124^\circ, 125^\circ)$, $(26^\circ, 27^\circ)$. Segments below this virtual line form a loop, or eddy-like feature centred at $(124^\circ, 25.5^\circ)$ that covers latitudes down to 24.5° and longitudes down to 123° . In the south, segments that are projected on the dense filamentary region, also known as the MCLD 123.5+24.9 cloud, appear to be parallel to the axis of the filament and its surrounding less dense gas.

Contrary to this picture, the most prominent feature of the much denser Taurus Molecular Cloud (the B211/B213 filament) appears perpendicular to the plane-of-the-sky magnetic field. However, a comparison between the two most prominent features of these clouds could be misleading, as they exhibit quite different characteristics. First, the B211 region is known to contain dense cores and YSOs (e.g. Kenyon, Gomez & Whitney 2008), while in MCLD 123.5+24.9 Ward-Thompson et al. (2010) found that all cores were starless and marginally gravitationally bound. Using the same *Herschel* data, Wagle et al. (2015) found that the same cores studied by Ward-Thompson et al. (2010) are most likely gravitationally unbound. So the two regions show a qualitatively different star forming activity. Second, the column density of MCLD 123.5+24.9 is comparable to that of the faint striations found in Taurus, $N(\text{H}_2) \sim 10^{21} \text{cm}^{-2}$, – an order of magnitude less than B211/B213, which has $N(\text{H}_2) > 10^{22} \text{cm}^{-2}$ (for column densities see André et al. 2010; Palmeirim et al. 2013, respectively).

A pattern similar to that found in the striations region of the map has been observed in the Taurus Molecular Cloud. Chapman et al. (2010) have shown that in a diffuse region far away from the main body of the cloud (around

¹ The *Herschel* image was available at the *Herschel* Gould Belt Survey online archive (André et al. 2010).

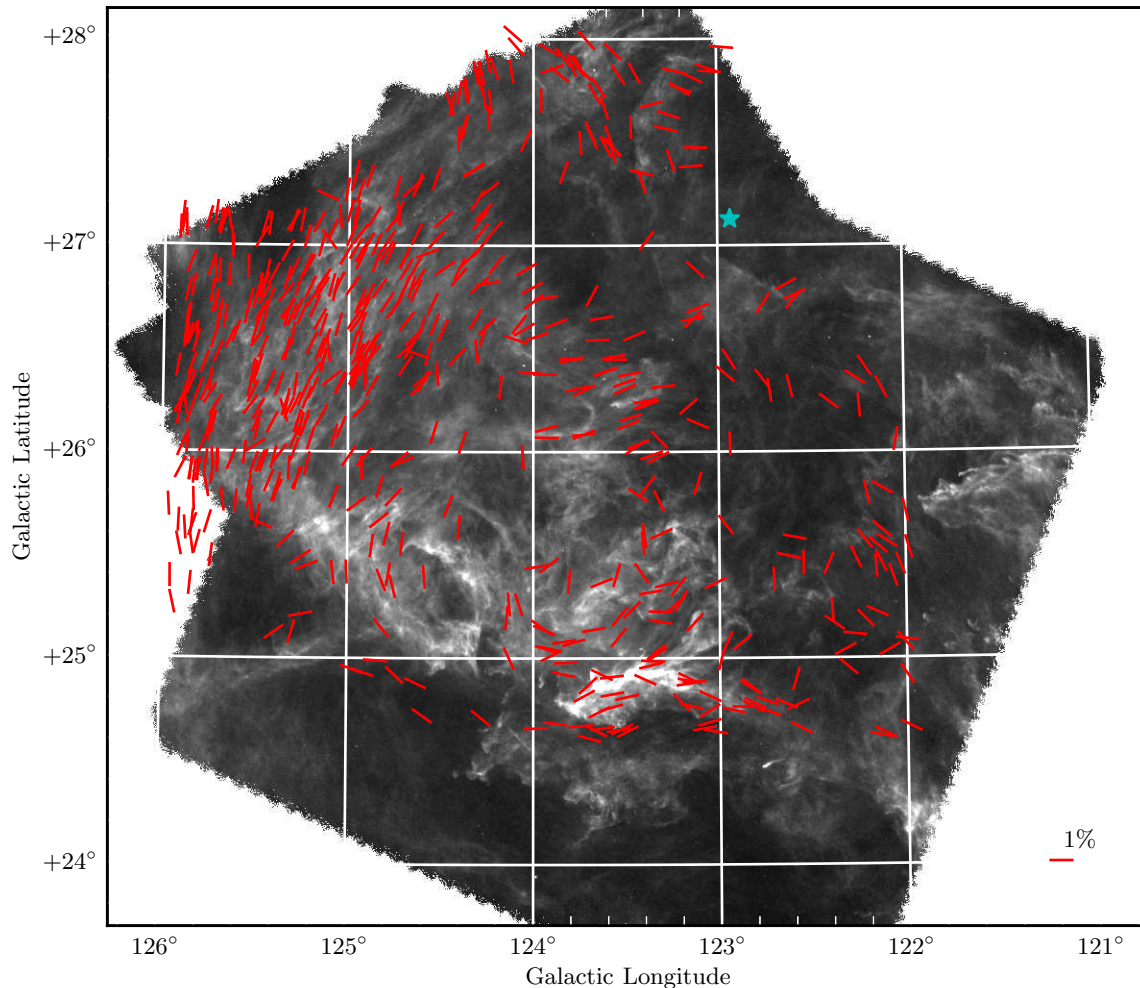


Figure 16. Polarization segments over plotted on top of the $250\ \mu\text{m}$ dust emission image of the Polaris Flare from the online archive of the *Herschel* Gould Belt Survey. The length of each segment is proportional to the debiased fractional linear polarization (p_d) of the star. The horizontal segment at the bottom right corner is for scale. The blue star marks the position of the North Celestial Pole.

$4^{\text{h}}50^{\text{m}}, 27^{\circ}$), striations appear aligned with optical and near-infrared polarization segments. The pattern is also present in the densest part of the cloud, around the B211/B213 filamentary region. Palmeirim et al. (2013) found that faint striations on both sides of the B211 filament were parallel to the plane-of-the-sky magnetic field and perpendicular to the filament. They thus speculated that material could be accreting along field lines and onto the filament. In spite of these similarities, the striations seen in the Polaris Flare do not appear connected to a much denser filamentary structure and have an order of magnitude lower column density; $N(\text{H}_2) \sim 10^{20}\text{cm}^{-2}$ (André et al. 2010); than those in Taurus; $N(\text{H}_2) \sim 10^{21}\text{cm}^{-2}$ (Goldsmith et al. 2008; Palmeirim et al. 2013).

A detailed, quantitative comparison of the magnetic field as revealed by the map to the dust emission features in the *Herschel* data will be presented in a follow-up paper. Such a study will allow for a thorough investigation of the implications of our findings on the filamentary model of star formation (André et al. 2014).

The general structure of the plane-of-the-sky magnetic

field in this cloud agrees qualitatively with that inferred from the polarized emission seen by the Planck satellite (Planck collaboration XX 2015). Even though the resolution of the presented map does not allow for a detailed comparison, the orientation of the ordered east part is in fair agreement with that seen in our map. Also, the central-southwest part in the Planck map does show a discontinuity of the projected field orientation that could be a sign of the loop that we observe.

The proximity of the cloud suggests that the level of contamination by dust foreground to the cloud is insignificant. Stars lying in front of the cloud will most likely exhibit very low polarization ($\ll 1\%$) and so would not comply with the p/σ_p threshold, thus they would not affect the map.

The distribution of stars for which we have reliable polarization measurements is not uniform. Segments at higher galactic latitude and longitude are denser than at the lower part of the map. Fig. 17 shows the number of stars in the map binned across the entire observed region. The bin size corresponds to that of the field of view. The brighter regions (containing more stars per bin) are in the area with ordered

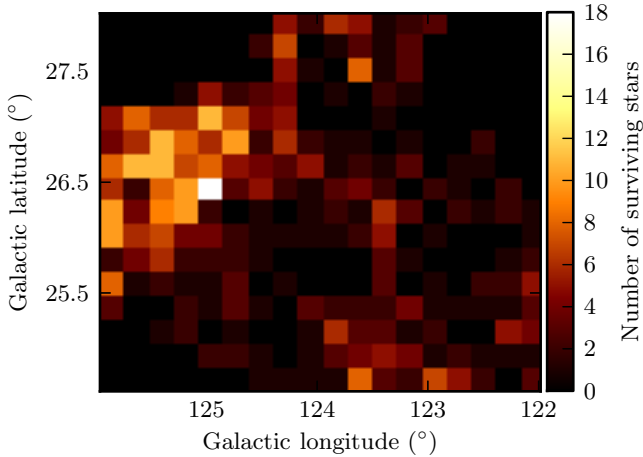


Figure 17. Number of stars in the map per field across the sky. The size of the bins corresponds to that of the field of view. The non-uniformity is a result of the p/σ_p cut.

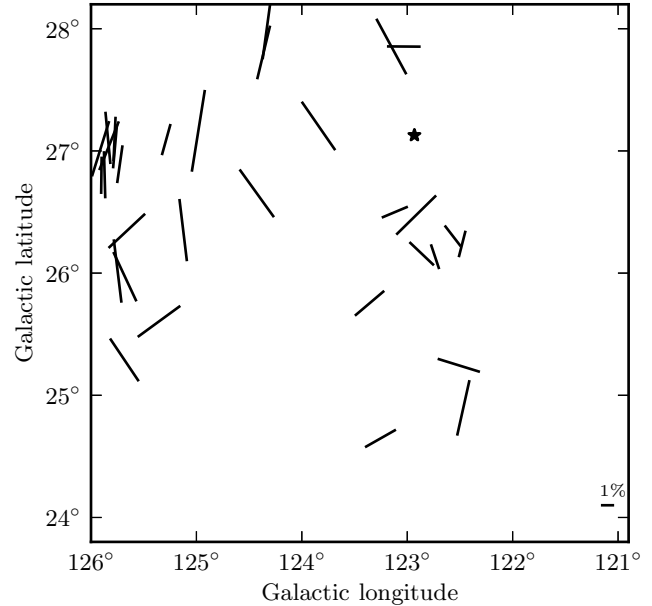


Figure 19. Polarization segments of stars above the $P-A_V$ line shown in Fig. 15. The black star shows the position of the North Celestial Pole while the horizontal segment in the bottom right sets the scale (1%).

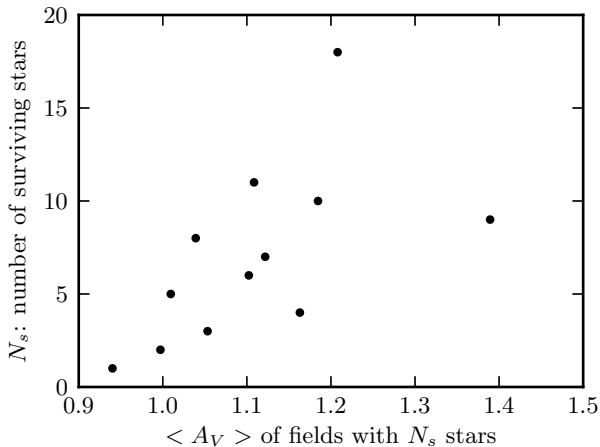


Figure 18. Number of stars (N_s) in Fig. 16 versus mean A_V in all fields with N_s .

plane-of-the-sky magnetic field. This non-uniformity is not due to variations in the stellar density across the observed region. It appears as a result of the p/σ_p cut. We find no correlation between this pattern and observing conditions (i.e. seeing, elevation, moon phase). For all fields with a given number of surviving stars (N_s), we calculate the mean extinction $\langle A_V \rangle$. There is a clear correlation between the two, as can be seen in Fig. 18. We find that the Pearson correlation coefficient between these two sets is 0.59. We therefore conclude that this effect is most likely not the result of some systematic error, but that of the cloud properties. A possibility that could give rise to this effect is a magnetic field whose direction changes from mostly on the plane-of-the-sky in the upper left part of the map, to having a more pronounced component along the line of sight towards the lower right.

Potentially intrinsically polarized sources

We plot the polarization segments of sources above the dashed line of Fig. 15 separately in Fig. 19 to be easily distinguished from those whose polarization is primarily affected by the magnetic field of the cloud. The length of the polarization segment of each star is proportional to its debiased p . The orientations of some segments are correlated with the general direction of the plane-of-the-sky magnetic field map of Fig. 16. This is not surprising since the $p-A_V$ line is empirical. Therefore our choice of setting a threshold based on that line is conservative.

We investigate the possibility that a number of the 32 sources falling above the $p_d - A_V$ line in Fig. 15 could be quasar candidates. Multi-wavelength data in this region are sparse, so cross-correlations with our sample were not particularly fertile. The low resolution of radio data renders direct identification of optical counterparts impractical. For most highly polarized sources (over the $p_d - A_V$ line) we only managed to find data from the USNOB and 2MASS catalogs. Kouzuma & Yamaoka (2010) presented the color properties of quasar and AGN candidates in the 2MASS catalog. They demonstrated that candidates can be found preferentially at certain regions of color-color diagrams. None of our sources seem to fit into this category. It should be noted, though, that these values have not been redshift-corrected.

Table 2. Reliable polarization measurements in the Polaris Flare region shown in Fig. 16 (full table online).

R.A.	Dec	$l(^{\circ})$	$b(^{\circ})$	p_d (%)	σ_p (%)	$\chi(^{\circ})$	$\sigma_{\chi} (^{\circ})$	$\theta_{gal} (^{\circ})$
0.31831	89.14655	122.72530	26.29510	1.5	0.6	- 3	6	9
1.14158	88.29658	122.54890	25.45990	0.9	0.4	-10	9	1
1.68599	88.42759	122.59422	25.58533	0.7	0.3	68	10	78
1.75619	89.21122	122.76249	26.35422	0.7	0.3	27	10	37
3.27012	88.34173	122.62601	25.49291	0.9	0.3	68	9	77

5 SUMMARY

We have presented optical linear polarization measurements of stars projected on the Polaris Flare field. These measurements reveal the plane-of-the-sky magnetic field structure of the cloud. The observations span about 10 deg^2 of the region and have been conducted with the RoboPol polarimeter in the R-band. We presented adjustments to the automated data reduction pipeline that were necessary for the analysis of sources in the entire $13' \times 13'$ field of view. We have investigated possible sources of systematic errors and have presented our methods for correcting for each one.

We have produced a map of 609 polarization segments showing the magnetic field structure of the cloud as projected on the plane of the sky. The median debiased p is 1.3%. The projected field shows a complicated, ordered structure throughout the map. To the top left part of the map, the field is aligned with the striations seen in dust emission. The bottom right parts show the presence of an eddy-like feature spanning roughly 2 degrees in diameter. Our results compare well with the Planck map of polarized emission of the cloud. The distribution of stars with reliable polarization measurements across the field is not uniform, with most stars lying in the top left of the region. This is most likely due to the intrinsic properties of the magnetic field structure.

ACKNOWLEDGEMENTS

We thank A. Kougentakis, G. Paterakis, and A. Steiakaki, the technical team of the Skinakas Observatory. The University of Crete group acknowledges support by the ‘‘RoboPol’’ project, implemented under the ‘‘ARISTEIA’’ Action of the ‘‘OPERATIONAL PROGRAMME EDUCATION AND LIFELONG LEARNING’’ and is co-funded by the European Social Fund (ESF) and Greek National Resources. The Nicolaus Copernicus University group acknowledges support from the Polish National Science Centre (PNSC), grant number 2011/01/B/ST9/04618. This research is supported in part by NASA grants NNX11A043G and NSF grant AST-1109911. V.P. acknowledges support by the European Commission Seventh Framework Programme (FP7) through the Marie Curie Career Integration Grant PCIG10-GA-2011-304001 ‘‘JetPop’’. K.T. acknowledges support by FP7 through the Marie Curie Career Integration Grant PCIG-GA-2011-293531 ‘‘SFOnset’’. V.P., E.A., I.M., K.T., and J.A.Z. would like to acknowledge partial support from the EU FP7 Grant PIRSES-GA-2012-31578 ‘‘EuroCal’’. I.M. is supported for this research through a stipend from the International Max Planck Research School (IMPRS) for Astronomy and Astrophysics at the Universities of Bonn

and Cologne. M.B. acknowledges support from the International Fulbright Science and Technology Award. T.H. was supported by the Academy of Finland project number 267324. The RoboPol collaboration acknowledges observations support from the Skinakas Observatory, operated jointly by the University of Crete and the Foundation for Research and Technology - Hellas. Support from MPIfR, PNSC, the Caltech Optical Observatories, and IUCAA for the design and construction of the RoboPol polarimeter is also acknowledged. This research has used data from the *Herschel* Gould Belt Survey (HGBS) project (<http://gouldbelt-herschel.cea.fr>). The HGBS is a *Herschel* Key Programme jointly carried out by SPIRE Specialist Astronomy Group 3 (SAG 3), scientists of several institutes in the PACS Consortium (CEA Saclay, INAF-IFSI Rome and INAF-Arcetri, KU Leuven, MPIA Heidelberg), and scientists of the *Herschel* Science Center (HSC). This research has used data from the NASA/IPAC Extragalactic Database (NED) which is operated by the Jet Propulsion Laboratory, California Institute of Technology, under contract with the National Aeronautics and Space Administration. This research has made use of the SIMBAD database, operated at CDS, Strasbourg, France as well as the VizieR catalogue access tool, CDS, Strasbourg, France. This work made use of APLpy, an open-source plotting package for Python hosted at <http://aplpy.github.com>, Astropy, a community-developed core Python package for Astronomy (Astropy 2013), matplotlib, a Python library for publication quality graphics (Hunter 2007) and the Python library SciPy (SciPy 2001). We would like to thank Malte Tewes for his help with the alipy package.

REFERENCES

- André Ph. et al., 2010, *A&A*, 518, L102
 André Ph. et al., 2014, *Protostars and Planets VI*, University of Arizona Press, preprint arXiv:1312.6232
 Astropy Collaboration, 2013, *A&A*, 558, A33
 Bailey J., Hough J. H., 1982, *PASP*, 94, 618
 Berdyugin A., Piirola V., Teerikorpi P., 2014, *A&A*, 561, A24
 Chapman N. L., Goldsmith P. F., Pineda J. L., Clemens D. P., Li D., Krčo M., 2011, *ApJ*, 741, 21
 Eswaraiiah C., Pandey A. K., Maheswar G., Medhi B. J., Pandey J. C., Ojha D. K., Chen W. P., 2011, *MNRAS*, 411, 1418
 Falgarone, E., Panis, J. F., Heithausen, A., Pérault M., Stutzki J., Puget J.-L., Bensch F., 1998, *A&A*, 331, 669
 Goldsmith P. F., Heyer M., Narayanan G., Snell R., Li D., Brunt C., 2008, *ApJ*, 680, 428
 Heiles C., 1984, *ApJS*, 55, 585

- Heiles C., 2000, *AJ*, 119, 923
- Heithausen A., Stacy J. G., de Vries H. W., Mebold U., Thaddeus P., 1993, *A&A*, 268, 265
- Hily-Blant P., Falgarone E., 2009, *A&A*, 500, L29
- Howell S. B., 1989, *PASP*, 101, 616
- Hunter J. D., 2007, *Computing In Science & Engineering*, 9, 3, 90
- Jones E., Oliphant T., Peterson P., 2001, www.scipy.org
- Kenyon S. J., Gomez M., Whitney B. A., 2008, *Handbook of Star Forming Regions* vol. 1, 405-458, 405
- King O. G. et al., 2014, *MNRAS*, 442, 1706
- King O. G. et al., 2014, *MNRAS*, 445, L114
- Kouzuma S., Yamaoka H., 2010, *Proceedings of the International Astronomical Union, IAU Symposium*, 267, 113
- Miville-Deschênes et al., 2010, *A&A*, 518, L104
- Palmeirim P. et al., 2013, *A&A*, 550, A38
- Pavlidou V. et al., 2014, *MNRAS*, 442, 1693
- Planck collaboration XIX, 2015, *A&A*, 576, A104
- Planck collaboration XX, 2015, *A&A*, 576, A105
- Reig P., Blinov D., Papadakis I., Kylafis N., Tassis K., 2014, *MNRAS*, 445, 4235
- Schlafly E. F., et al. 2014, *ApJ*, 786, 29
- Schlafly E. F., Finkbeiner D. P., 2011, *ApJ*, 737, 103
- Schmidt G.D., Elston R., Lupie O.L., 1992, *AJ*, 104, 1563
- Serkowski K., Mathewson D. S., Ford V. L., 1975, *ApJ*, 196, 261
- Simmons J. F. L., Stewart B. G., 1985, *A&A*, 142, 100
- Stephens I. W., Looney L. W., Dowell C. D., Vaillancourt J. E., Tassis K., 2011, *ApJ*, 728, 99
- Ulmer M. P., Baity W. A., Wheaton W. A., Peterson L. E., 1973, *ApJ*, 184, L117
- Vaillancourt J. E., 2006, *PASP*, 118, 1340
- Wagle G. A., Troland T. H., Ferland G. J., Abel N. P., 2015, preprint (arXiv:1504.06311)
- Ward-Thompson D., et al., 2010, *A&A*, 518L, 92